Design of a Magnetic Actuated Fully Insertable Robotic Camera System for Single-Incision Laparoscopic Surgery

Xiaolong Liu, Gregory J. Mancini, Yong Guan, and Jindong Tan

Abstract—This paper presents the design of a novel insertable robotic capsule camera system for single-incision laparoscopic surgery. This design features a unified mechanism for anchoring, navigating, and rotating a fully insertable camera by externally generated rotational magnetic field. The design is inspired by the spherical motor concept where the external stator generates anchoring and rotational magnetic field to control the motion of the insertable robotic capsule camera. The insertable camera body, which has no active locomotion mechanism onboard, is capsulated in a one-piece housing with two ring-shaped tail-end magnets and one cylindrical central magnet embedded onboard as a rotor. The stator positioned outside an abdominal cavity consists of both permanent magnets and electromagnetic coils for generating reliable rotational magnetic field. The initial prototype results in a compact insertable camera robot with a 12.7 mm diameter and a 68 mm length. The design concepts are analyzed theoretically and verified experimentally. The experiments validate that the proposed camera robot design provides reliable camera fixation and locomotion capabilities under various testing conditions.

Index Terms—Camera robot, laparoscopic surgery, magnetic actuation.

I. INTRODUCTION

SINGLE-INCISION laparoscopic surgery (SILS) is a popular minimally invasive surgery technique. Its benefits include less bleeding, less postoperative pain, fast incision recovery, and better cosmetic results compared with multiport surgeries [1]. However, a single incision limits the manipulation and triangulation of surgical instruments, especially for a conventional long-stick laparoscopic camera. To solve this problem, fully insertable laparoscopic cameras have been developed [2], [3].

X. Liu is with the Department of Mechanical, Aerospace, and Biomedical Engineering, University of Tennessee, Knoxville, TN 37996 USA, and also with Smokie Robotics, Inc., Knoxville, TN 37996 USA (e-mail: xliu57@utk.edu).

G. J. Mancini is with the Graduate School of Medicine, University of Tennessee, Knoxville, TN 37996 USA (e-mail: GMancini@mc.utmck.edu).

Y. Guan is with the College of Information Engineering, Capital Normal University, Beijing 100048, China (e-mail: guanyong@mail.cnu.edu.cn).

J. Tan is with the Department of Mechanical, Aerospace, and Biomedical Engineering, University of Tennessee, Knoxville, TN 37996 USA (e-mail: tan@utk.edu).

Color versions of one or more of the figures in this paper are available online at http://ieeexplore.ieee.org.

Digital Object Identifier 10.1109/TMECH.2015.2506148

One major challenge to design a fully insertable laparoscopic camera is the development of its actuation functions, which are 1) fixation that holds the cameras in stable positions; 2) translation that repositions the cameras; and 3) rotation that manipulates the cameras to desired orientations. The existing laparoscopic camera designs have addressed separate or partial-function-combined actuation mechanisms. A tethered laparoscopic camera, which can be fixed against an abdominal wall by suturing, used two DC motors and peripheral mechanisms for its rotation control [4]. A wireless laparoscopic camera with a needle for fixation was developed to actuate its rotational function (pan and tilt motions) by using two onboard motors [5]. Due to the repositioning difficulty by the fixations of suturing and needle piercing, magnetic anchoring was applied to address this issue. External permanent magnets (EPMs) were utilized to couple with internal permanent magnets (IPMs) inside cameras for fixation, translation and pan motion, while onboard motors have to be reserved to generate tilt motion [6]–[8].

Related robot designs, such as endoscopic robots, were developed to travel along gastrointestinal (GI) tracts [9], [10], or be manipulated in fluid-filled lumens and/or soft tissues [11]. An endoscopic capsule robot with four IPMs onboard was demonstrated in [12], which utilized a single cylindrical EPM mounted on a robot arm to guide the robot to inspect GI tracts. A drug-release robot was reported in [13], in which the drug-release and locomotion mechanisms were designed by adopting a rolling cylinder EPM placed externally and a pair of axially magnetized IPMs inside the robot. Because of the low controllability by using EPMs, electromagnetic coils were applied to achieve flexible endoscopic robot control. A three-axis Helmholtz coils system was proposed to create rolling/rotating motions for a drug-release robot [14]. An actuation mechanism of a capsule robot was achieved by wirelessly powering onboard motors and electronics with a coil vest [15]. A spiral structure warped capsule robot was proposed in [16], which applied an externally rotational magnetic field to actuate the robot with an IPM onboard. A microrobot, which was made of permanent magnets for delicate retinal surgery, was designed to be actuated by eight electromagnetic coils for pose and force/torque control [17].

A major difference of the actuation requirements between a laparoscopic camera robot and an endoscopic camera robot is that the fixation function is trivial for an endoscopic camera robot. However, for a laparoscopic camera robot, the fixation and rotation functions have to cooperatively work all the time to keep the camera being stably fixed in position when a rotational motion is actuated. Considering the separate actuation mechanisms of the state-of-the-art laparoscopic camera robots and the restriction to utilize the designs of the endoscopic camera robots, there
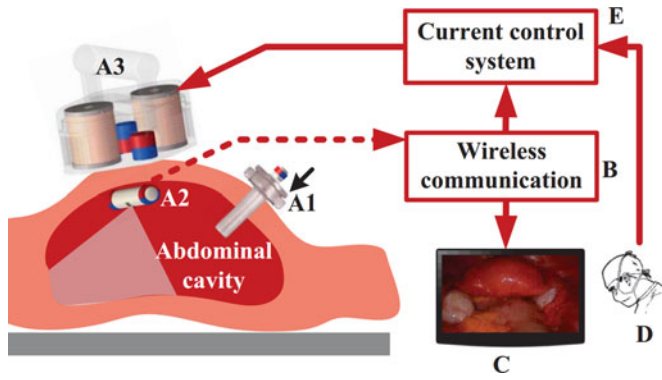
Fig. 1.   System overview of the magnetic actuated camera robot.

Fig. 2.   Conceptual design of the proposed camera robot system.

is a need to develop a unified fixation, translation, and rotation mechanism for a laparoscopic camera robot.

Motivated by various spherical motor concepts [18], [19], this paper proposes an innovative actuation mechanism design of wireless laparoscopic camera robots that can be anchored (fixation), navigated (translation), and orientated (rotation) wirelessly with a single rigid body. In our prior work [20], [21], two designs have been proposed. The first prototype arranged tiny cylindrical IPMs on a semispherical dome surface inside the camera robot to serve as a rotor, and applied spherically arranged electromagnetic coils to serve as a stator [20]. Although this design benefits from its small size, simple fabrication, and unified actuation, for stable motion control, the stator needed at least 5-A current inputs, which resulted in coil overheating. The second one proposed a conceptual design that applied 17 flatly arranged coils as a stator and three diametrically magnetized cylindrical magnets as a rotor [21]. The simulation results proved the feasibility of the second design. However, the experimental testings of the fabricated design showed that the current control of the 17 coils required a complex algorithm, which caused poor control reliability.

In this paper, we propose a significantly improved actuation mechanism for a laparoscopic camera robot based on our prior work [21]. As shown in the conceptual illustration of Fig. 1, the camera robot can be inserted into the gas filled body cavity via the incision. The wireless robot can be navigated from the incision to a desired spot to illuminate and visualize the target surgical area. The key component and innovation of the camera robot is the permanent magnetic driving unit, which is referred to as a rotor, driven externally by an especially designed magnetic stator, as illustrated in Fig. 2. The rotor, consisting of three IPMs that are distributed at tail-ends and central housing of the camera robot, can be magnetically coupled to a stator placed externally against or close to the dermal surface. The fixation, translation, and rotation functions of the rotor can be achieved by adjusting the magnetic field from the stator.

The contributions of this paper include: 1) a novel unified actuation mechanism design, including the robot housing, the rotor IPMs, and the parametric investigations of the stator EPMs and coils for providing reliable actuation capabilities; 2) models of the interactive magnetic forces and torques between the rotor and the stator for real-time motion control; and 3) a demonstration of the fabricated prototype, with a thorough ac-
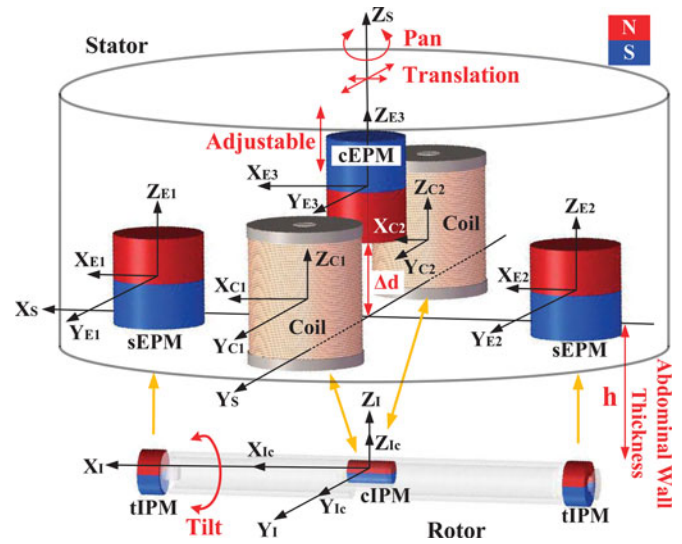
tuation capabilities investigation under controlled experimental environments.

II. SYSTEM OVERVIEW AND CONCEPTUAL DESIGN

A. System Overview

Fig. 1 illustrates an application scenario of the proposed laparoscopic camera robot. To insert the camera robot (A1) into the patient's abdominal cavity, a trocar is first applied. The robot is introduced into the abdominal cavity with nonferrous metal surgical forceps, and fixed against the abdominal wall at an initial position (A2) by a stator (A3). A surgeon (D) sends signals of desired robot poses to the current control system (E) by using a user interface. The camera robot at (A2) sends imaging information to the display terminal (C) through the wireless communication module (B).

B. Conceptual Design

The objective of this paper is to design a unified active locomotion mechanism for a fully insertable wireless laparoscopic camera robot with no onboard motors. As conceptually illustrated in Fig. 2, the locomotion mechanism consists of 1) a rotor with two tail-end IPMs (tIPMs) and one central IPM (cIPM), and 2) a stator with two coils, two side EPMs (sEPMs), and one central EPM (cEPM). In the stator that placed externally against an abdominal wall, the EPMs and the coils are orthogonally arranged. In the rotor that pushed against an abdominal wall internally, the robot body can rotate freely related to the ring-shaped tIPMs that have unchanged orientations with respect to the stator, and the diametrically magnetized cylindrical cIPM is fixed with the robot body.

The stator-rotor mechanism is designed to enable orientation (rotational control) and navigation (translational control), in addition to the compensation of the gravity of the camera (fixation control). The robot orientation consists of pan motion and tilt motion. The pan motion requires torque along Z_I-axis of the robot, and the tilt motion control requires torque along X_I-axis.

The robot navigation requires forces along X_I-, Y_I-, Z_I-axes, with the force along Z_I-axis providing fixation of the robot against the abdominal wall. The robot navigation control is provided by moving the stator along the dermal surface with the attractive forces between the sEPMs and the tIPMs. A spinning motion of the stator along Z_S can actuate the robot pan motion by coupling the magnetic field of the sEPMs and the tIPMs. Due to the dominated magnetic field from the sEPMs at the location of the cIPM, the cEPM with its north pole pointing downside is used to eliminate the influence from the sEPMs on the cIPM by adjusting the cEPM displacement along Z_S. In this way, the robot tilt motion can be effectively actuated by the magnetic coupling between the coils and the cIPM.

The open-ended research problem of this paper is twofold: 1) the design of the stator-rotor locomotion mechanism for the camera robot; and 2) the control model of the robot tilt motion. The detailed discussions are presented in Sections III and IV.

III. DESIGN OF ROBOT ACTUATION MECHANISM

The working environments of the laparoscopic camera robot are insufflated abdominal cavities and abdominal walls. To insert the robot into an abdominal cavity, the diameter of the robot should adapt to the 12–15 mm diameter of a standard trocar. Considering the normal thickness of an abdominal wall that ranges from 20 to 40 mm [22], the actuation mechanism design should be able to provide sufficient actuation capabilities under this working range.

A. Rotor Design

1) Robot Housing: The robot housing is designed to host onboard electronics and a cIPM by using a 12.7 mm outer diameter (OD) and 10 mm inner diameter (ID) tube. A small cylindrical housing is built in the middle of the tube to fix the cIPM. Two shafts connected with the robot housing caps are designed to support the tIPMs. This design enables the robot housing and the tIPMs to be separate pieces when they rotate along the robot axis. The robot length is an important parameter to be determined because it affects the torque on the cIPM from the tIPMs. To reserve sufficient space for onboard electronics and avoid overly lengthy device, the candidate robot length ranges from 50 to 100 mm. The final length selection depends on the robot actuation performance, which is described in Section III-B.

2) Rotor Magnets: The rotor magnets used in the design are diametrically magnetized. The reason to choose this type of magnet is twofold: first, ring-shaped/cylindrical magnets can be well fitted into the capsule-shaped robot; and second, diametrically magnetized magnets can be efficiently actuated by external magnetic fields. Due to the restricted diameter of the robot, two ring-shaped magnets with ODs of 12.7 mm, IDs of 4.75 mm, and thicknesses of 6.35 mm are selected to serve as tIPMs to maximize the magnetic anchoring performance on the rotor side. The cIPM applies a cylindrical magnet with a 6.35 mm diameter and a 12.7 mm length to fit in the robot housing. Based on the determined parameters of the rotor design, a stator design can, thus, be studied for optimizing the robot actuation performance.
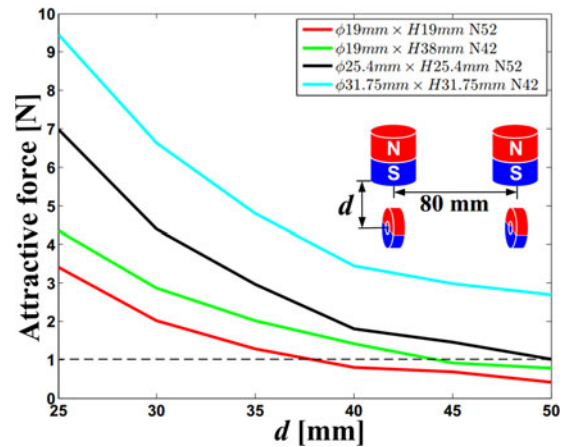

Fig. 3. Fixation forces are investigated by using four pairs of candidate sEPMs and a pair of tIPMs. The evaluation is conducted under 25–50-mm rotor-to-stator distances and the distance between the sEPMs at 80 mm.

B. Stator Design

The stator design aims at providing reliable magnetic field to manipulate the camera robot for fixation, translation, and rotation (pan and tilt motions). Due to the multiple desired actuation functions and the complex composition of the stator magnetic field, which is generated from two coils and three EPMs, the analysis of the stator magnetic design has to be decoupled for each specific actuation function. The key issue of the stator design is to decouple the pan motion and the tilt motion. A cEPM is designed to reduce the dominated magnetic field by the sEPMs in the working space of the cIPM. In this way, the coils are enabled to actuate the tilt motion of the rotor. The fixation, translation, and pan motion are actuated by the magnetic coupling between the sEPMs and the tIPMs.

The stator design follows three steps: first, the sEPMs should be designed to provide sufficient fixation force, translation force, and pan motion torque for the camera robot; second, parameters and configurations of the coils have to be optimized to balance the coil volumes and magnetic field strength; and third, the central axis field of the stator has to be designed by using a cEPM to decouple the pan motion and the tilt motion of the camera robot. The design analysis of the stator in this section is conducted by COMSOL Multiphysics 5.0 (COMSOL, Inc., Sweden).

1) sEPMs of the Stator: According to our preliminary experimental study, a set of axially magnetized cylindrical magnets serve as sEPM candidates. The dimensions and materials of the magnets are illustrated in the legend of Fig. 3. To investigate the attractive force between the sEPMs and the tIPMs, the robot length is temporarily determined at 80 mm which is approximately the middle point of the desired length range 50–100 mm. Since the normal range of an abdominal wall thickness is 20–40 mm, the range of the rotor-to-stator distance d, which is the distance between the bottom surface of the stator and the symmetric axis of the rotor, is estimated as 30–50 mm. Fig. 3 shows the simulation results of the attractive forces between different sets of the sEPMs and the tIPMs under the rotor-to-stator distance ranging from 30 to 50 mm. With the
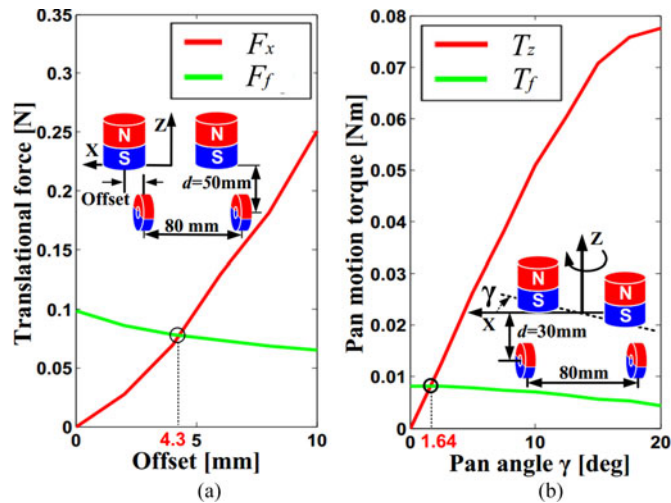
Fig. 4. Translational force and pan motion torque investigation. (a) Comparison result of translational force F_x between a stator and a rotor in *X*-direction, and frictional force F_f in $-X$-direction with the stator offset distance ranging from 0 to 10 mm. (b) Comparison result of the pan motion torque T_z and the frictional torque T_f against the pan motion.
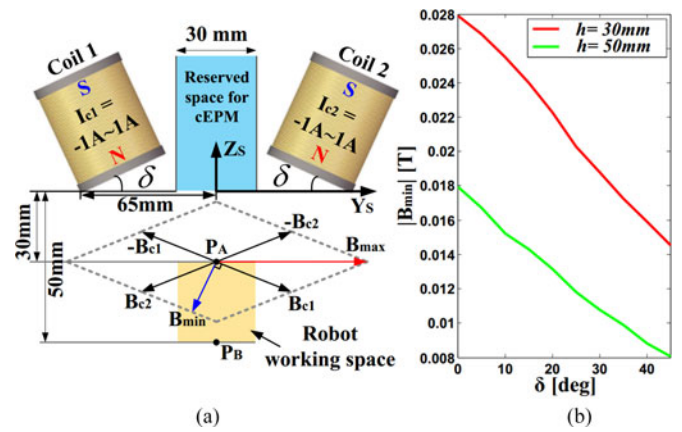

Fig. 5. Configurations of electromagnetic coils in the stator. (a) Setup for testing the coils with δ angle to generate an optimal magnetic field in the robot working space. $\mathbf{B}_{\min}$ and $\mathbf{B}_{\max}$ represent the minimum and the maximum magnetic field strength in a rotational magnetic field generated by the coils. (b) Relationship between the coils tilt angle δ and $\mathbf{B}_{\min}$.

estimated total robot weight that is under 30 g, the magnet with the dimension $\phi 25.4$ mm $\times H 25.4$ mm, which generates more than 4 N force at 30 mm and 1 N at 50 mm, can provide reliable fixation force with maximum contact compression about 0.5 psi against an abdominal wall. This pressure is much smaller than the safe threshold 3.45 psi for preventing undesired histological damages [23].

Based on the selected sEPMs, the translation and pan motion of the rotor are investigated in Fig. 4. Fig. 4(a) shows the simulation results of the translational motion with offsets ranging from 0 to 10 mm between the sEPMs and the tIPMs under 50-mm rotor-to-stator distance. The result shows that the translational force F_x in *X*-direction can overcome the frictional force F_f in $-X$-direction after the offset distance reaches 4.3 mm. The robot-tissue frictional force F_f is calculated by $F_f = \mu(F_z - mg)$, where μ is the static frictional coefficient that sets as 0.1 according to [24]; F_z is the attractive force generated from the magnetic coupling between the sEPMs and the tIPMs in Fig. 5(a); mg represents the gravity of the robotic camera. Fig. 4(b) shows that the sEPMs can provide sufficient pan motion torque T_z along the central axis of the stator to overcome the frictional torque T_f after a relative rotational angle $\gamma = 1.64°$ is reached.

2) Coils of the Stator: The coil dimension design is based on the intensive experimental studies in our prior work [20], [21] to determine a compact size of the coils with sufficient magnetic field strength. The experiments indicate a coil with 50 mm height, 50 mm OD, 10 mm ID, and an iron core with 60 mm height is optimal. The winding wire used in the coils is AWG23 copper wire with 2000 turns. For the safety consideration, the input current of the coils is limited to 1.5 A for preventing coil overheating.

To optimize the utilization of the coil, magnetic field in the robot working space, as illustrated in the yellow area of Fig. 5(a), the configurations that include the distance between the coils, and the tilt angle δ need to be studied. The minimal

distance between the two coils is determined by the volume of a cEPM. According to the dimensions of the sEPMs (25.4 mm diameter, 25.4 mm height), a cylindrical space with 30 mm in diameter, as shown in the blue region of Fig. 5(a), is reserved for a cEPM to balance the central axis field of the stator. The tilt angle δ of the coils is used to adjust the magnetic field performance. Due to the desire of having a compact stator design, the coil pivot points used to achieve tilt angles are set at ± 65 mm on the Y_S-axis by considering the 50 mm diameters of the coils.

To determine an optimal δ angle $\mathbf{B}_{\min}$, which is a minimum composed magnetic field by the coils, is used to quantify the performance of δ angle. As illustrated in Fig. 5(a), $\mathbf{B}_{c1}$ and $\mathbf{B}_{c2}$ are the magnetic fields generated by the coil 1 and the coil 2, respectively. The rhombus demonstrates the region of possible composed magnetic field by limiting the current inputs at 1 A.

Fig. 5(b) shows the $|\mathbf{B}_{\min}|$ values at the working space boundary points $\mathbf{P}_A$ and $\mathbf{P}_B$, which represent the rotor-to-stator distance 30 and 50 mm, respectively. The magnetic field investigation is conducted by ranging δ angle from $0°$ to $45°$. The simulation results indicate that the optimal tilt angle δ is $0°$, which enables the coils to generate the maximum $|\mathbf{B}_{\min}|$.

3) Central Axis Field of the Stator: The purpose of designing the central axis field of the stator is to reduce the dominated field control by the sEPMs, and subsequently enables the coils to actuate the cIPM for tilt motion with an inversely positioned cEPM. The key problem of the central axis field design is to determine an acceptable range of magnetic field strength generated by the EPMs in the cIPM working space, as shown in Fig. 6(a). Under the designed range of magnetic field, the coils should be able to actuate the robot to achieve at least $60°$ tilt motion, which is sufficient for a laparoscopic visualization task.

To estimate an acceptable range of the central axis field $\mathbf{B}_{\mathrm{epm}}$, a static torque analysis of the robot tilt motion is conducted by considering the relations between $\mathbf{B}_{\mathrm{epm}}$ and T_{epm}. $T_{\mathrm{epm}} \in$
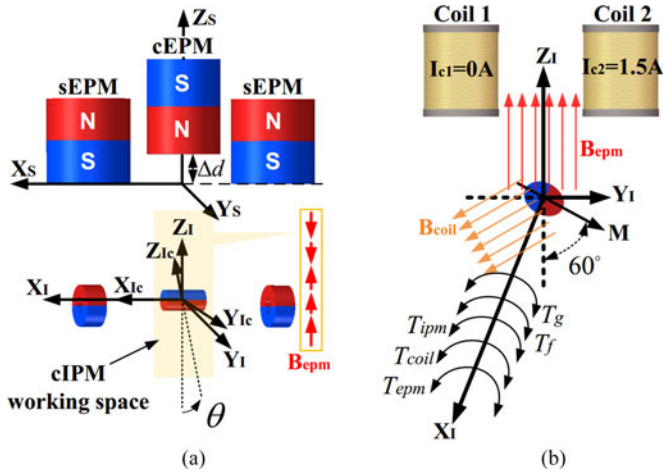
Fig. 6. Design of the central axis field of the stator. (a) Configuration of the cEPM and the EPMs magnetic field in the working space of the cIPM. (b) Analysis of the central axis field $\mathbf{B}_{\text{epm}}$.

TABLE I
CENTRAL AXIS MAGNETIC FIELD BOUNDARY $|\mathbf{B}_{\text{epm}}|$

Rotor-to-stator distance (mm)	Robot length (mm)		
	50	60	70
30	0.0416 T	0.0371 T	0.0361 T
50	0.0219 T	0.0179 T	0.0168 T
	Robot length (mm)		
	80	90	100
30	0.0334 T	0.0329 T	0.0328 T
50	0.0143 T	0.0139 T	0.0138 T

$\mathbb{R}^{1\times1}$ is the magnetic torque applied on the cIPM from the EPMs along X_I-axis. We assume that the cIPM is described by a body-attached magnetic moment $\mathbf{M} \in \mathbb{R}^{3\times1}$ with a constant magnitude in ampere square meter. The torque and force on the cIPM generated from the stator, in newton meters and newtons, respectively, can be expressed as

$$\mathbf{T} = \mathbf{M} \times \mathbf{B}, \qquad \mathbf{F} = (\mathbf{M} \cdot \nabla)\mathbf{B} \qquad (1)$$

where $\mathbf{B} \in \mathbb{R}^{3\times1}$ represents the magnetic field of the stator [25]. In accordance with (1), T_{epm} can be calculated by

$$T_{\text{epm}} = |\mathbf{B}_{\text{epm}}| \cdot |\mathbf{M}| \cdot \sin(\widehat{\mathbf{B}_{\text{epm}}, \mathbf{M}}). \qquad (2)$$

To guarantee that the robot can achieve at least $60°$ tilt angle, the boundary condition of T_{epm} is expressed by

$$T_{\text{epm}} + T_f \leq T_{\text{coil}} + T_{\text{ipm}} + T_g \qquad (3)$$

where T_f is a frictional torque generated between the abdominal wall and the robot; T_{coil} is the torque on the cIPM with $60°$ tilt angle by giving input current of the coil 2 as $1.5A$; T_{ipm} is the torque on the cIPM with $60°$ tilt angle from the tIPMs; and T_g is the gravity torque of the robot. The reason to put T_f on the left side of (3) is to develop a strict boundary to T_{epm}. The boundary condition (3) should be valid under 30–50-mm rotor-to-stator distances. The robot length, which determines the distance between the sEPMs, has a major impact on T_{ipm} and is evaluated in the range of 50–100 mm. Except T_{epm}, all the other torques in (3) are calculated by modeling the rotor and the stator in COMSOL. The boundary values of the central axis field $\mathbf{B}_{\text{epm}}$ are calculated according to the boundary values of T_{epm} and (2), as illustrated in Table I. The minimum boundary value of $|\mathbf{B}_{\text{epm}}|$ is 0.0138 T under the condition of the rotor-to-stator distance 50 mm, and the robot length 100 mm. Therefore, the central axis magnetic field of the stator can be bounded to $|\mathbf{B}_{\text{epm}}| < 0.0138$ T.

Under the guideline of the central axis field boundary developed above, the cEPM can be designed. As illustrated in Fig. 6(a), the central axis field $\mathbf{B}_{\text{epm}}$ changes its direction as the rotor-to-stator distance increases. To control the tilt motion

of the robot, $\mathbf{B}_{\text{epm}}$ with $+Z_I$-direction is desired in the cIPM working space as illustrated in Fig. 6(b) because the magnetic field with this direction can help the coils to actuate the cIPM for achieving a larger tilt angle. To reserve sufficient space for on-board electronics, the distance between the centers of the tIPMs is determined at 60 mm. The distance between the sEPMs is subsequently determined. By using the trial and error method, the cEPM is designed as an axially magnetized cylindrical magnet with 22.22 mm in diameter, 28.57 mm in height, and an offset distance $\Delta d = 5\text{--}10$ mm in $+Z_S$-direction. The range of the central axis field with the designed cEPM is evaluated by COMSOL under rotor-to-stator distance 30–50 mm. The simulation results in $|\bar{\mathbf{B}}_{\text{epm}}| \in [0.0014\text{ T}, 0.00497\text{ T}]$, which has a unidirectional field point in $+Z_S$-direction, and is within the acceptable central axis field boundary $|\mathbf{B}_{\text{epm}}| < 0.0138$ T.

IV. CONTROL MODEL OF THE ROBOT TILT MOTION

This section aims at developing a control model for the robot tilt motion activated by the coils. The objective can be achieved by 1) analyzing the stator magnetic field, and 2) modeling the robot dynamics with the magnetic force/torque between the rotor and the stator, and the frictional force/torque between the robot and an abdominal wall.

To clarify the relationship between the stator and the rotor, coordinate systems are defined in Fig. 2, and explained as follows:

1) $\Sigma_{Ei}\{X_{Ei}, Y_{Ei}, Z_{Ei}\}$ represents the coordinate systems of the EPMs, $i = 1, 2, 3$.
2) $\Sigma_{Cj}\{X_{Cj}, Y_{Cj}, Z_{Cj}\}$ represents the coordinate systems of the coils, $j = 1, 2$.
3) $\Sigma_S\{X_S, Y_S, Z_S\}$ and $\Sigma_I\{X_I, Y_I, Z_I\}$ represent the internal coordinates of the stator and the rotor, respectively.
4) $\Sigma_{Ic}\{X_{Ic}, Y_{Ic}, Z_{Ic}\}$ represents the body attached coordinate systems of the cIPM.

A. Magnetic Field Analysis of the Stator

Due to the fixed relative positions of the EPMs and the coils, the stator magnetic field can be calculated by superimposing the magnetic fields from the EPMs and the coils [21].

1) EPM Magnetic Field: Inspired by Kok-Meng and Hungsun [26], the EPMs can be represented by a magnetic dipole array, as shown in Fig. 7(a). The magnetized direction is along $+Z$-axis, and the diameter and length of the magnet are a and L, respectively. The positive and negative magnetic charges are
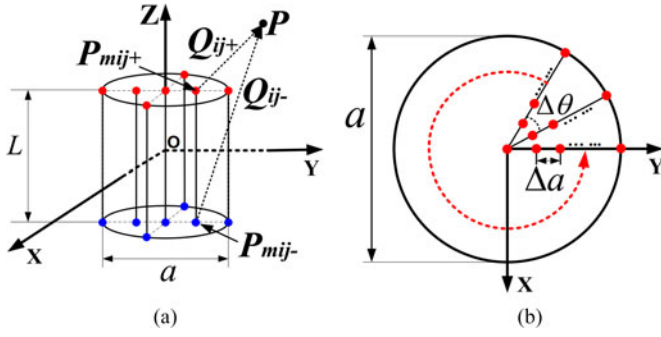
Fig. 7. EPM magnetic field modeling. (a) Multiple-pair magnetic dipoles of an EPM. L represents the distance between positive and negative magnetic charges. a represents the diameter of the cylinder space where the magnetic dipoles are distributed. $\mathbf{P}$ denotes a spacial point in the coordinate frame $\Sigma(X, Y, Z)$. $\mathbf{P}_{\mathrm{mij+}}$ and $\mathbf{P}_{\mathrm{mij-}}$ represent the locations of positive and negative magnetic charges of the ijth magnetic dipole. $\mathbf{Q}_{ij+}$ and $\mathbf{Q}_{ij-}$ represent the vectors from $\mathbf{P}_{\mathrm{mij+}}$ to $\mathbf{P}$ and from $\mathbf{P}_{\mathrm{mij-}}$ to $\mathbf{P}$, respectively. (b) Magnetic charge distribution on the positive charge surface. Δa represents an interval distance of adjacent magnetic charges along a radial direction. $\Delta \theta$ represents an interval angle between radial sampling lines.

distributed on the top and bottom surfaces. The number and the arrangement of the magnetic changes on the surfaces determine the accuracy of the magnetic field model. Fig. 7(b) shows the magnetic charge arrangement on one surface. Eleven magnetic changes are evenly sampled starting at ($x = 0$, $y = 0$), along +Y-direction. The interval distance Δa between two adjacent charges is calculated as $a/10$. Then, the magnetic charge sampling line on +Y-axis rotates around Z-axis with a sampling interval angle $\Delta \theta$ as $\pi/6$. Because the 121 magnetic charges are symmetrically distributed around Z-axis, only a quarter of the magnetic dipoles need to be estimated by the fitting data, which is obtained from FEM numerical magnetic field results.

By summarizing all the magnetic dipoles, the magnetic flux density of an EPM is expressed as

$$\mathbf{B}_e = \frac{\mu_0}{4\pi} m_0 \Gamma_{00} + \frac{\mu_0}{4\pi} \sum_{i=1}^{K_m} \sum_{j=1}^{N_m} m_{ij} \Gamma_{ij} \quad (4)$$

$$\Gamma_{ij} = \frac{\mathbf{Q}_{ij+}}{|\mathbf{Q}_{ij+}|^3} - \frac{\mathbf{Q}_{ij-}}{|\mathbf{Q}_{ij-}|^3} \quad (5)$$

where m_{ij} is the strength of the ijth magnetic dipole, and m_0 is the strength of the magnetic dipole at the center; $K_m = 10$ denotes the number of magnetic dipoles radially, and $N_m = 12$ is the number of magnetic dipoles for a single loop; and $\mathbf{Q}_{ij+/-}$ represents a vector from the location of positive/negative magnetic charge $\mathbf{P}_{\mathrm{mij+}}/\mathbf{P}_{\mathrm{mij-}}$ to a point $\mathbf{P}$ in space.

2) Coil Magnetic Field: It has been experimentally proved in [17] that the magnetic flux density of an iron-core coil has a linear relationship with its input current. To develop the magnetic field model for an iron-core coil, Kummer *et al.*[17] estimate the parameter with one pair of magnetic dipoles by using the magnetic field data generated from FEM solutions of a unit-current coil. Compared with a single pair of magnetic dipoles, a multiple-dipole model, which has been used for estimating EPM models above, has more abilities to achieve an accurate model. Thus, to derive the model of the magnetic field of an

iron-core coil, (4) is applied to estimate a unit-current magnetic field. The relationship between an input current of a coil and the generated magnetic flux density is formulated by

$$\mathbf{B}_c = \mathbf{B}_c^u I_c \quad (6)$$

where $\mathbf{B}_c^u$ has the same formulation as $\mathbf{B}_e$ in (4), but the fitting data are generated from a unit-current coil; and I_c is the input current of the coil.

3) Superimposed Magnetic Field: Since the magnetic field models of the EPMs and the coils are separately developed, a superimposed magnetic field of the stator can thus be formulated. Recalling the coordinate systems demonstrated in Fig. 2, $\mathbf{R}_{Ei}$, $\mathbf{T}_{Ei}$ and $\mathbf{R}_{Cj}$, $\mathbf{T}_{Cj}$ represent the rotation matrices and translation vectors from Σ_S to Σ_{Ei} and from Σ_S to Σ_{Cj}, respectively. The superimposed magnetic field of the stator can be expressed in (7) by using (4) and (6)

$$\mathbf{B}_s(\mathbf{P}_s) = \sum_{i=1}^{3} \mathbf{R}_{Ei} \mathbf{B}_e^i(\mathbf{P}_i) + \sum_{j=1}^{2} \mathbf{R}_{Cj} \mathbf{B}_c^u(\mathbf{P}_j) I_{cj} \quad (7)$$

where $\mathbf{B}_e^i$ denotes the magnetic flux density of the ith EPM; $\mathbf{P}$ represents the coordinates in frame Σ_S; and $\mathbf{P}_i$, $\mathbf{P}_j$ are the transferred coordinates of $\mathbf{P}_s$ from Σ_S to Σ_{Ei} and Σ_{Cj} by using $\mathbf{P}_i = \mathbf{R}_{Ei}^T \mathbf{P}_s - \mathbf{R}_{Ei}^T \mathbf{T}_{Ei}$ and $\mathbf{P}_j = \mathbf{R}_{Cj}^T \mathbf{P}_s - \mathbf{R}_{Cj}^T \mathbf{T}_{Cj}$.

To investigate the validity of the model of the stator magnetic field, the displacement of the cEPM was set as $\Delta d = 5$ mm. Considering the working space of the cIPM, 20 mm × 20 mm magnetic field testing regions were designed on both the $X_S Z_S$ plane and the $Z_S Y_S$ plane for evaluating the EPM field and the coil field, respectively, as shown in Fig. 8(a) and (d). The comparison results of the EPMs magnetic field generated by our developed model and an FEM model are shown Fig. 8(b) and (c). Similarly, Fig. 8(e) and (f) shows the comparison results of the magnetic field generated from the unit-current coil by using the magnetic field model and an FEM model separately. To evaluate the results quantitatively, the sampled magnetic field data, which are the black dots shown in Fig. 8(b), (c) and (e), (f), were applied with 2 mm intervals in the testing regions for both the EPMs and the coil. The average errors for the comparison results of the EPMs and the coils are 7.85% and 1.23%, respectively. The accuracies of the developed magnetic field models were further improved by providing more experimental data for (4) and (6) in Section V-B.

B. Control With Electromagnetic Coils

The robot tilt motion is activated by the magnetic coupling between the coils and the cIPM. I_{c1} and I_{c2} are represented as the current inputs of the coils, and θ represents the rotational angle of the robot tilt motion. The robot dynamics need to be studied for developing the relationship between the control inputs I_{c1}, I_{c2} and the output θ.

Fig. 6(b) shows the dynamic analysis of the robot tilt motion. The torques that affect the tilt motion along X_I include 1) T_s which is the combination of T_{epm} and T_{coil} on the cIPM from the EPMs and the coils of the stator; 2) T_{ipm} which is the magnetic torque on the cIPM from the tIPMs along X_I; and 3) T_f and T_g which are the frictional torque of the robot–tissue interaction and the torque due to the robot gravity along X_I. The bold fonts
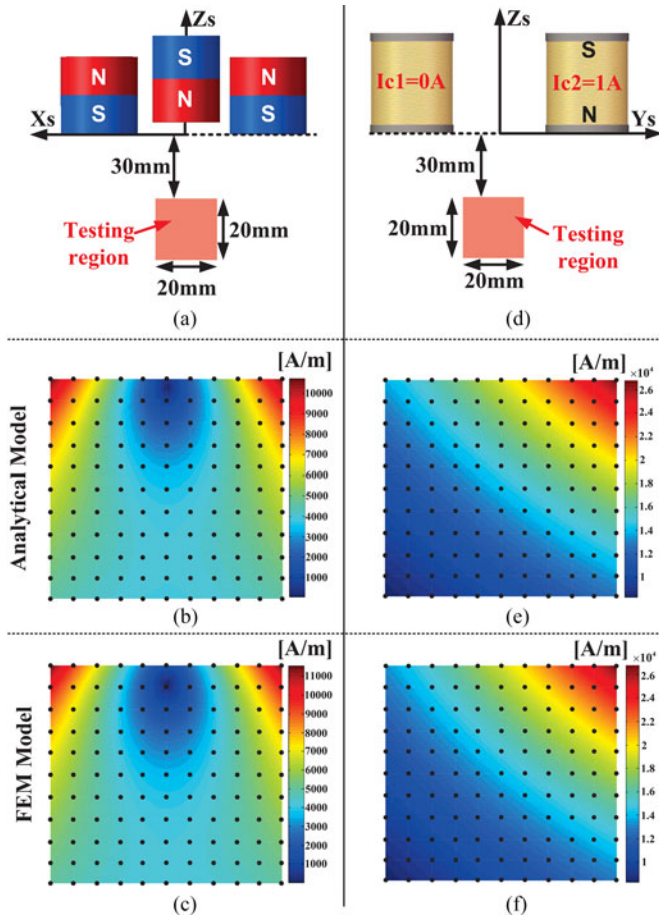
Fig. 8. Stator magnetic field modeling and evaluations. (a) Configuration for testing the composed magnetic field of the EPMs. (b), (c) Magnetic fields of the EPMs in the testing region of (a) calculated by the magnetic field model and FEM method separately. (d) Configuration for testing the magnetic field of the coils. (e), (f) Magnetic fields of the coil in the testing region of (d). (e) is generated by the magnetic field model, and (f) is developed by the FEM method.

$\mathbf{T}_s, \mathbf{T}_{\text{ipm}}, \mathbf{T}_f$, and $\mathbf{T}_g$ are used to represent the torque vectors with the components along X_I, Y_I, Z_I.

Combining (1) and (7), the torque on the cIPM generated from the stator, in newton meters, can be expressed as

$$\mathbf{T}_s = \underbrace{\mathbf{M} \times \left(\sum \mathbf{R}_{Ei} \mathbf{B}_e^i \right)}_{\mathbf{E}} + \underbrace{\left(\mathbf{M} \times \mathbf{R}_{C1} \mathbf{B}_c^u \right)}_{\mathbf{C}_1} I_{c1}$$
$$+ \underbrace{\left(\mathbf{M} \times \mathbf{R}_{C2} \mathbf{B}_c^u \right)}_{\mathbf{C}_2} I_{c2} \qquad (8)$$

where $\mathbf{E} \in \mathbb{R}^{3\times1}$ denotes the torque from the EPMs, $i = 1, 2, 3$; $\mathbf{C}_1 \in \mathbb{R}^{3\times1}$ and $\mathbf{C}_2 \in \mathbb{R}^{3\times1}$ denote the unit-current torques from the coils. Benefiting from the magnetic field model in (4), $\mathbf{E}, \mathbf{C}_1$, and $\mathbf{C}_2$ can be computed in real time.

The nonzero components in $\mathbf{T}_f$ and $\mathbf{T}_{\text{ipm}}$ are the x-components represented by T_f and T_{ipm}. T_f is determined by F_{attr}, which is the attractive force between the stator and the rotor. Due to the reduced magnetic field of the EPMs in the cIPM working space, the magnetic coupling between the stator and the cIPM has a minor contribution which is less than 7% of

the total attractive force according to our simulation. To reduce the complexity of the system control, this trivial contribution of the attractive force F_{attr} is neglected. As $F_{\text{attr}} = f_1(h)$ and $T_{\text{ipm}} = f_2(\theta)$ are functions of an abdominal wall thickness h and the robot tilt angle θ, respectively, f_1 and f_2 can be modeled by polynomial approximation

$$f_1(h) = \sum_{k=1}^{n+1} \eta_k h^{n-k+1}, \qquad f_2(\theta) = \sum_{k=1}^{m+1} \xi_k \theta^{m-k+1} \qquad (9)$$

where η_k and ξ_k are the polynomial coefficients to be determined by experimental data; n and m denote the degrees of f_1 and f_2.

The reason to use different methods to represent $\mathbf{T}_s$ and $\mathbf{T}_f$, $\mathbf{T}_{\text{ipm}}$ is that the assumption made in (1) cannot hold well for modeling $\mathbf{T}_f$ and $\mathbf{T}_{\text{ipm}}$ according to the preliminary comparison results between model data and experimental data. The reason of the modeling disagreement for $\mathbf{T}_f$ and $\mathbf{T}_{\text{ipm}}$ is twofold: 1) the magnetic field distribution of a tIPM is more complicated than a unified magnetic field distribution; and 2) the distance between the adjacent IPMs (about 20 mm) and the distance between the EPMs and the IPMs (It depends on an abdominal wall thickness, e.g., 30 mm.) are much smaller than that between the two coils and the cIPM (about 42 mm). The magnetic interactions between the EPMs and the IPMs for $\mathbf{T}_f$ and $\mathbf{T}_{\text{ipm}}$ are more close to near-field interactions which further reject the assumption in (1).

By representing $\boldsymbol{\omega} = [\dot{\theta}, 0, 0]^T$ as the angular velocity of the robot tilt motion, the dynamic model can be formulated in Σ_I as

$$\mathbf{T}_s + \mathbf{T}_{\text{ipm}} + \mathbf{T}_f + \mathbf{T}_g = \mathbf{I}'\dot{\boldsymbol{\omega}} + \boldsymbol{\omega} \times \mathbf{I}'\boldsymbol{\omega} \qquad (10)$$

where $\mathbf{I} \in \mathbb{R}^{3\times3}$ is the moment of inertia in the body attached frame Σ_{I_c}; $\mathbf{R}_I^{I_c} \in \mathbb{R}^{3\times3}$ is the rotational matrix from Σ_I to Σ_{I_c}; and $\mathbf{I}' = \mathbf{R}_I^{I_c} \cdot \mathbf{I} \cdot (\mathbf{R}_I^{I_c})^T$ is the moment of inertia of the rigid body in Σ_I.

Since the tilt motion is actuated along the X_I-axis, only the x components need to be considered in (10). By substituting (8) and (9) into (10), the dynamic equation is reformulated as

$$E_x + C_{1x}I_{c1} + C_{2x}I_{c2} + T_{\text{ipm}} + \mu(F_{\text{attr}} - mg)r_f$$
$$+ mgr_g \sin\theta = a_{11}\ddot{\theta} \qquad (11)$$

where E_x, C_{1x}, C_{2x} are the x components in $\mathbf{E}, \mathbf{C}_1$, and $\mathbf{C}_2$, respectively; μ is the frictional coefficient between the robot and an abdominal wall; mg represents the gravity of the robot; r_f and r_g denote the lever arms of the friction force and the gravity force to generate T_f and T_g; and a_{11} denotes the element of first row, first column in $\mathbf{I}$.

To generate a desired tilt angle for the robot, the coil current inputs I_{c1} and I_{c2} can be found by applying pseudoinverse to

$$\mathbf{C}_x \mathbf{I}_c = G \qquad (12)$$

where $\mathbf{C}_x = [C_{1x}, C_{2x}] \in \mathbb{R}^{1\times2}$; $\mathbf{I}_c = [I_{c1}, I_{c2}]^T \in \mathbb{R}^{2\times1}$; G represents the summation of the remaining terms in (11). Because $\mathbf{C}_x$ has a full row rank, the solution of the current input vector $\mathbf{I}_c$ can be calculated by using

$$\mathbf{I}_c = \mathbf{C}_x^T (\mathbf{C}_x \mathbf{C}_x^T)^{-1} G. \qquad (13)$$
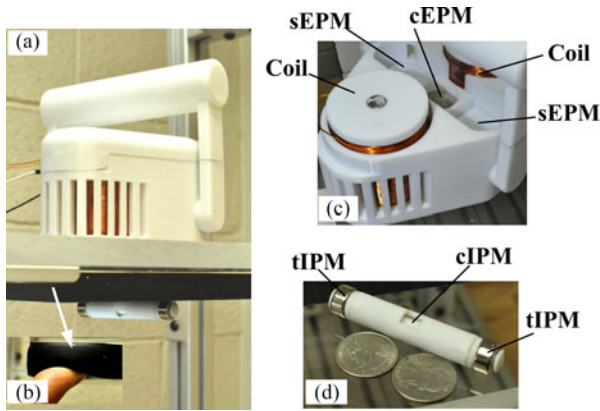
Fig. 9. Experimental environment and the fabricated capsule robot system: (a) Experiment setups for evaluating the robot locomotion capabilities; (b) simulated abdominal wall tissue made by a viscoelastic material; (c) stator design; and (d) rotor design.

V. EXPERIMENTAL VALIDATION

A. Prototype Fabrication and Experiment Platform Setup

1) Experiment Platform Setup: Fig. 9(a) shows the overview of the experimental environment. The robot system was fabricated by a 3-D prototyping machine (Fortus 400mc, Stratasys, Inc.). To simulate the viscoelastic properties of a real insufflated abdominal wall (average Young's modulus 32.5 kPa) [22], a viscoelastic material Durometer 40 (Young's modulus 27.57 kPa at 15% deflection, Sorbothane, Inc.) was applied as illustrated in Fig. 9(b). The initial abdominal wall thickness was 26 mm (tissue layer 15 mm, support layer 11 mm), which can be adjusted by increasing the distance between the stator and the support layer. The vertical displacement Δd of the cEPM can be manually adjusted at this stage. A silicone oil lubricated rotor–tissue contact layer with frictional coefficient about 0.1 was added to the bottom of the viscoelastic material for mimicking an internal abdominal wall surface [24].

2) Rotor and Stator Fabrication: Fig. 9(c) and (d) shows the prototype of the camera robot and the stator. The permanent magnets applied in the prototype are all from K&J Magnetics. The AWG23 cooper wires adopted in the coils are from TEMCo, and the iron-cores of the coils are made by EFI Alloy 50 from Ed Fagan. The space above the EPMs in the stator is reserved for the onboard electronics and the tetherless power supply of the stator.

3) Current Control System: A tethered current control system was developed by the PWM technique. The system consists of a microcontroller (STM32F4Discovery, STMicroelectronics, Inc.) to generate PWM signals, two PWM amplifiers (L6205 DMOS Full Bridge Driver, STMicroelectronics Inc.) to amplify the signals, a power supply for powering up the amplifiers, and a PC computer to send control command to the microcontroller via a serial communication.

B. Model Evaluation

1) Stator Magnetic Field: The models of the stator magnetic field developed in Section IV-A were validated by using hall effect sensors (CYL8405, ChenYang Technologies
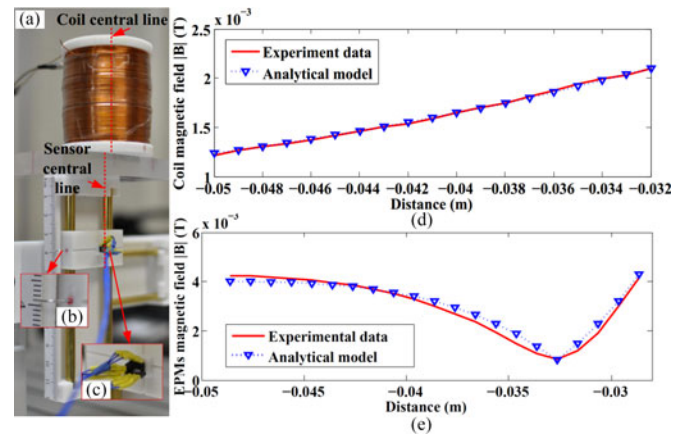

Fig. 10. Stator magnetic field experimental evaluation.

GmbH) with measuring range 0–64 mT and sensitivity about 50 mV/mT. The measured analog magnetic field signals were converted to digital signals with sensing resolution 0.01 mT by using a 16 bit ADC (ADS1115, Texas Instruments, Inc.). Due to the imperfection of the coil wrapping, the iron cores, and the permanent magnets, model calibration was performed by using experimental data. Fig. 10(a) shows the experiment platform for magnetic field validation which consists of a vertical moving track with a position indicator [see Fig. 10(b)], three hall effect sensors for three-axis sensing [see Fig. 10(c)], and a transparent support board for placing the coils or the EPMs at desired locations. Fig. 10(d) and (e) shows the magnetic flux density norm comparison results of the experimental data and the magnetic field models along the sensor central line for a single coil with unit-current input and the three EPMs with the vertical displacement of the cEPM as $\Delta d = 1$ mm. According to the configuration of the stator, the distance from the coil central line to the sensor central line was set as 40 mm for validating the coil magnetic field. For the EPMs, the sensor central line was set to coincide with the central line of the cEPM. The average errors of the magnetic field models demonstrated in Fig. 10(d) and (e) were 0.001% and 0.02%, respectively.

2) Magnetic Torque on the cIPM: Fig. 11(a) shows the experimental setup for evaluating $\mathbf{T}_s$ in (8). Due to the tilt motion generated along the camera axis, T_s which is the x component of $\mathbf{T}_s$ was measured by changing the current inputs of the coils I_{c1} and I_{c2}. A six-axis force/torque (F/T) sensor (HEX-58-RB-2000N, OptoForce, Inc.), as illustrated in Fig. 11(a)-④ with torque resolution $5e-4$ N · m along the shaft was applied. A cIPM was embedded in the camera housing [see Fig. 11(a)-⑤], which was connected to the F/T sensor with a shaft [see Fig. 11(a)-⑥]. The tilt angle of the camera housing was fixed at $0°$. The distance h between the stator and the camera was adjusted by a lifting mechanism [see Fig. 11(a)-①], and measured by a caliper [see Fig. 11(c)-⑨]. An aluminum board was used at the bottom surface of the lifting mechanism [see Fig. 11(a)-③] with relative magnetic permeability about 1. The input current I_{c1} was fixed at -1.5 A, while I_{c2} was linearly changed from -1.5 to 1.5 A. Fig. 12 shows the comparison results of experiment data and the model in (8) under stator-to-rotor distances 20, 30, and 40 mm. The average error of the model demonstrated in Fig. 12 was 0.0035%.
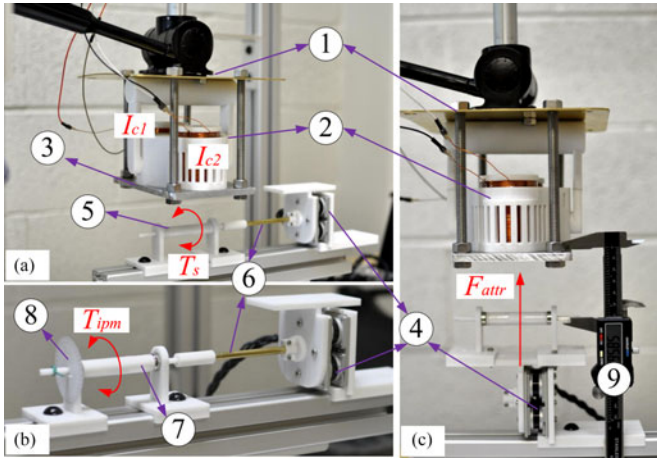
Fig. 11. Experiment configurations for evaluating the model of T_s in (a), estimating the polynomial coefficients of T_{ipm} in (b) and F_{attr} in (c). ①: stator lifting mechanism; ②: the stator; ③: the stator supporting board made by aluminum; ④: six-axis force/torque sensor; ⑤: camera housing with the cIPM inside, and without the tIPMs at the tail-ends; ⑥: shaft; ⑦: camera housing with the cIPM inside, and with the tIPMs at the tail-ends; ⑧: tilt angle indicator; ⑨: caliper for measuring the stator-to-rotor distance.
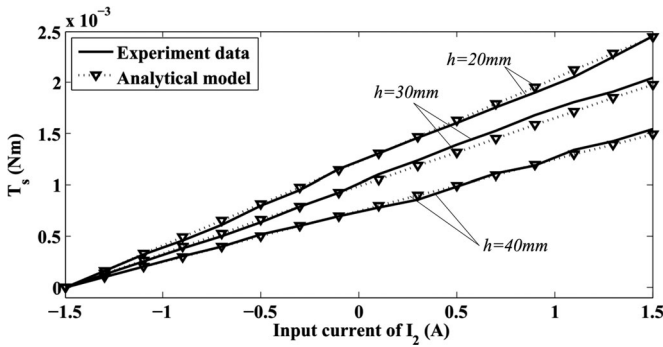

Fig. 12. Experimental evaluation of magnetic torque on the cIPM.

TABLE II
MAGNETIC TORQUE BETWEEN tIPMs AND cIPM T_{ipm}

θ (deg)	0	15	30	45	60	75	90
T_{ipm} (mN·m)	0	−0.76	−1.23	−1.53	−1.68	−1.85	−1.96

3) Polynomial Coefficients Estimation: Fig. 11(b) shows the experimental setup for measuring the magnetic torque T_{ipm} to estimate the polynomial coefficients in (9). Compared with the configuration of the camera housing in Fig. 11(a)-⑤, the configuration in Fig. 11(b)-⑦ applied two tIPMs with fixed orientations at both ends of the camera housing. The tilt angle of the cIPM was indicated by an angle indicator as illustrated in Fig. 11(b)-⑧. After a tilt angle was set, the shaft at the sensor side was fastened by the screws to hold the angle.

Table II shows the T_{ipm} experiment data by changing the tilt angle from 0 to 90° with 15° interval. The estimated polynomial coefficients for T_{ipm} are $\xi_1 = 0.0247$, $\xi_2 = -0.1176$,

TABLE III
STATOR/ROTOR ATTRACTIVE MAGNETIC FORCE

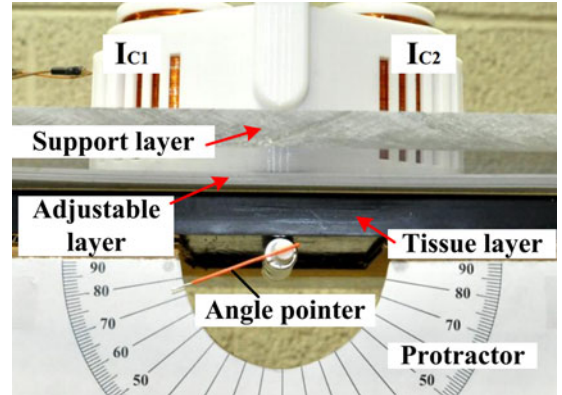| h (mm)	Δd (mm)	$F_{\mathrm{attr}}(N)$	ΔF (N)
20	11	3.978	±0.034
25	8	2.590	±0.034
30	4	1.626	±0.034
35	2	0.916	±0.034
40	1	0.544	±0.034
45	0	0.442	±0.034
50	0	0.340	±0.034

Fig. 13. Experimental setup for the open-loop control of the camera tilt motion.

$\xi_3 = 0.2298$, $\xi_4 = -0.4801$, $\xi_5 = -1.5159$ with a fitting error 0.76% at the fourth-degree polynomial [$m = 4$ in (9)].

Fig. 11(c) demonstrates the experimental setup for measuring the magnetic attractive force F_{attr} to estimate the polynomial coefficients in (9). Table III shows the attractive force F_{attr} between the stator and the rotor with respect to stator-to-rotor distance h sampled from 20 to 50 mm. The values in the column of Δd show the optimal displacements of the cEPM that enable minimal magnetic field from the EPMs on the cIPM. ΔF represents the maximum influence on the attractive force by activating the coils in the stator. The experiment data validates that the magnetic force contribution from the coils is minor compared with the magnetic force from the EPMs. A fourth-degree polynomial curving fitting [$n = 4$ in (9)] was applied for F_{attr} to achieve a curve fitting error 1.66% with the coefficients $\eta_1 = -0.0498$, $\eta_2 = -0.1143$, $\eta_3 = 0.7364$, $\eta_4 = -1.0856$, $\eta_5 = 0.9237$.

C. Open-Loop Control of Tilt Motion

Fig. 13 shows the experimental setups for the camera robot tilt motion control by using (11). The simulated abdominal wall consisted of three types of layers: 1) the tissue layer lubricated with silicone oil; 2) support layer; and 3) adjustable layer, which was used for changing the total thickness of the abdominal wall. To indicate the tilt angles, a protractor and an angle pointer were applied.

Considering the candidate onboard electronics to be integrated in the camera robot, the moment of inertia matrix $\mathbf{I}$ of the robot was estimated by modeling it in SolidWorks2013
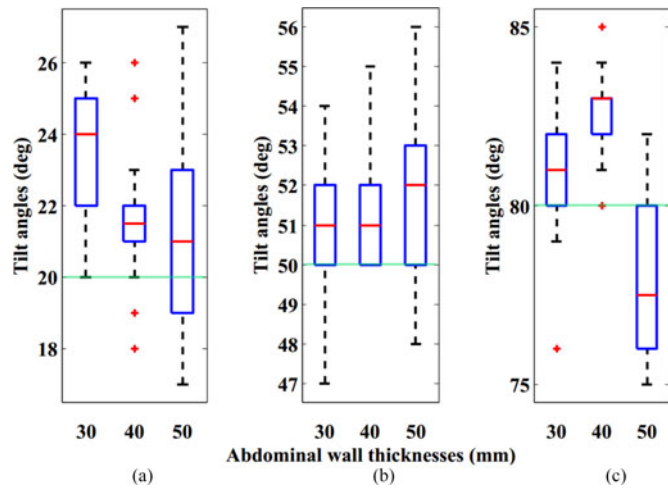
Fig. 14. Experimental results of the open-loop control of tilt motion. (a) Desired tilt angle $\theta_d = 20°$; (b) $\theta_d = 50°$; (c) $\theta_d = 80°$.

Fig. 15. Experimental results to demonstrate decoupled pan/tilt and translation/tilt motion.

(Dassault Systémes SolidWorks Corp.) as

$$\mathbf{I} = \begin{pmatrix} 0.174 & 0 & -0.003 \\ 0 & 3.473 & 0 \\ 0 & 0 & 3.469 \end{pmatrix} \quad (14)$$

where the unit of each element in $\mathbf{I}$ is $\text{kg} \cdot \text{mm}^2$. The other parameters used in (11) were estimated or measured as $\mu = 0.1$, $r_f = 4$ mm, and $r_g = 1.5$ mm. Extra weights were filled in the camera housing to simulate the full load of onboard electronics with the total weight of the camera robot as $mg = 0.26$ N.

To control the tilt motion with (11), fifth-order desired trajectories, which are smooth at the angular acceleration level, were generated by initializing the robot tilt angles as $0°$ and setting the desired tilt angles θ_d. The control current inputs I_{c1} and I_{c2} were computed by (13) in real time.

Fig. 14 shows the experimental results of the open-loop control of the camera tilt motion by setting the desired tilt angles as $20°$, $50°$, and $80°$, which are illustrated by the green lines in Fig. 14(a)–(c), respectively. This experiment was grouped by 30, 40, and 50 mm abdominal wall thicknesses. For each group and each desired tilt angle, the control process was implemented by 30 trials. The box-and-whisker plots indicate that the tilt angle errors fell in $\pm 7°$. The tilt angle control for $\theta_d = 50°$ in Fig. 14(b) was better behaved than in (a) and (c) with no single sample considered as extremes. Fig. 14(c) demonstrates that camera tilt angle can be successfully controlled up to $80°$ which is sufficient for visualization tasks of abdominal cavities.

D. Decoupled Pan/Tilt and Translation/Tilt Motion

Fig. 15 shows the experimental results that illustrate the decoupled pan/tilt and translation/tilt motion control for the camera system. To record tilt angles, a triaxial accelerometer (LIS331HH, STMicroelectronics, Inc.) was applied inside the dummy camera. The experiment was conducted by setting fixed tilt angles during pan motion and translation motion, and setting the simulated abdominal wall thickness as 40 mm. The pan
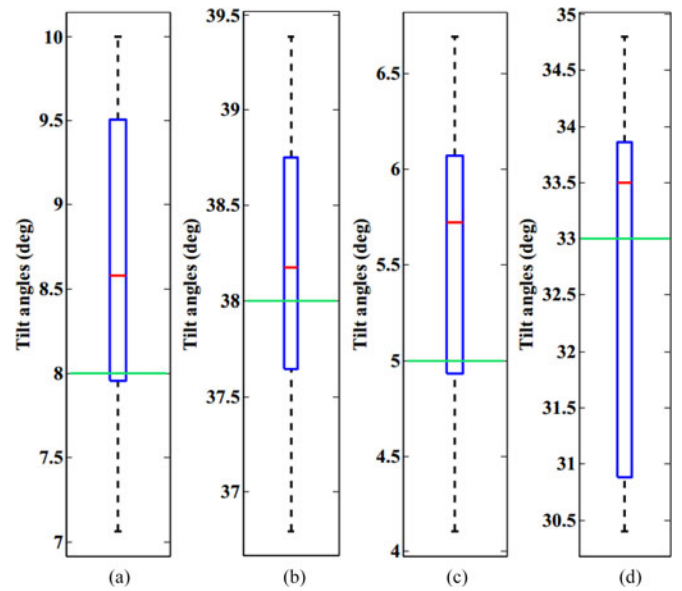
motion took about 9 s to achieve $360°$. The translation motion took about 5 s to travel 30 cm horizontally.

Fig. 15(a) and (b) shows the decoupled pan/tilt motion experiments by fixing tilt angles as $8°$ and $38°$, respectively. Fig. 15(c) and (d) shows the decoupled translation/tilt motion experiments by fixing tilt angles as $5°$ and $33°$, respectively. The impacts on the tilt angles from pan motion and translation motion are within $\pm 2°$ and $\pm 3°$, respectively.

VI. CONCLUSION

In this paper, a spherical motor inspired actuation mechanism for a fully insertable laparoscopic camera robot is presented. The actuation mechanism, which consists of an insertable rotor and an external stator, provides a unified camera robot locomotion control. Fixation, translation, and rotation functions are unified into a capsule design of insertable body, which is controlled by adjusting rotational magnetic field from the external stator. The experiments showed that the system provide reliable anchoring, translation, $360°$ continuous pan motion control, and fine tilt motion control up to $80°$ under the conditions of 30–50 mm simulated abdominal wall thicknesses. Pan and tilt motion can be simultaneously controlled in a decoupled way, which enables a flexible motion control of the camera robot to illuminate and visualize a target surgical area.

REFERENCES

[1] M. Saidy, M. Tessier, and D. Tessier, "Single-incision laparoscopic surger–hype or reality: A historical control study," *Perm J.*, vol. 16, no. 1, pp. 47–50, 2012.
[2] P. Swain, R. Austin, K. Bally, and R. Trusty, "Development and testing of a tethered, independent camera for notes and single-site laparoscopic procedures," *Surg. Endosc.*, vol. 24, no. 8, pp. 2013–2021, 2010.
[3] J. Cadeddu, R. Fernandez, M. Desai, R. Bergs, C. Tracy, S. Tang, P. Rao, M. Desai, and D. Scott, "Novel magnetically guided intra-abdominal camera to facilitate laparoendoscopic single-site surgery: Initial human experience," *Surg. Endosc.*, vol. 23, no. 8, pp. 1894–1899, 2009.

[4] T. Hu, K. Allen, J. Hogle, and L. Fowler, "Insertable surgical imaging device with pan, tilt, zoom, and lighting," *Int. J. Robot. Res.*, vol. 28, no. 10, pp. 1373–1386, 2009.

[5] C. Castro, S. Smith, A. Alqassis, T. ketterl, S. Yu, S. Ross, A. Rosemurgy, P. Savage, and R. Gitlin, "A wireless robot for networked laparoscopy," *IEEE Trans. Biomed. Eng.*, vol. 60, no. 4, pp. 930–936, Apr. 2013.

[6] S. Platt, J. Hawks, and M. Rentschler, "Vision and task assistance using modular wireless in vivo surgical robots," *IEEE Trans. Biomed. Eng.*, vol. 56, no. 6, pp. 1700–1710, Jun. 2009.

[7] M. Simi, M. Silvestri, C. Cavallotti, M. Vatteroni, P. Valdastri, A. Menciassi, and P. Dario, "Magnetically activated stereoscopic vision system for laparoendoscopic single-site surgery," *IEEE/ASME Trans. Mechatronics*, vol. 18, no. 3, pp. 1140–1151, Jun. 2013.

[8] M. Simi, G. Sardi, P. Valdastri, A. Menciassi, and P. Dario, "Magnetic levitation camera robot for endoscopic surgery," in *Proc. IEEE Int. Conf. Robot. Autom.*, 2011, pp. 5279–5284.

[9] J. Toennies, M. Simi, P. Valdastri, and R. Webster, "Swallowable medical devices for diagnosis and surgery: The state of the art," *J. Mech. Eng. Sci.*, vol. 224, no. 7, pp. 1397–1414, 2010.

[10] A. Moglia, A. Menciassi, P. Dario, and A. Cuschieri, "Capsule endoscopy: Progress update and challenges ahead," *Nature Rev. Gastroenterol. Hepatol.*, vol. 6, no. 1, pp. 353–362, 2009.

[11] B. J. Nelson, I. Kaliakatsos, and J. Abbott, "Microrobots for minimally invasive medicine," *Annu. Rev. Biomed. Eng.*, vol. 12, pp. 55–85, 2010.

[12] G. Ciuti, P. Valdastr, A. Menciassi, and P. Dario, "Robotic magnetic steering and locomotion of capsule endoscope for diagnostic and surgical endoluminal procedures," *Robotica*, vol. 28, no. 2, pp. 199–207, 2010.

[13] S. Yim and M. Sitti, "Design and rolling locomotion of a magnetically actuated soft capsule endoscope," *IEEE Trans. Robot.*, vol. 28, no. 1, pp. 183–194, Feb. 2012.

[14] S. H. Kim and K. Ishiyama, "Magnetic robot and manipulation for active-locomotion with targeted drug release," *IEEE/ASME Trans. Mechatronics*, vol. 19, no. 5, pp. 1651–1659, Oct. 2014.

[15] A. Uehara and K. Hoshina, "Capsule endoscope NORIKA system," *Minimally Invasive Ther. Allied Technol.*, vol. 12, no. 5, pp. 227–234, 2003.

[16] M. Sendoh, K. Ishiyama, and K.-I. Arai, "Fabrication of magnetic actuator for use in a capsule endoscope," *IEEE Trans. Magn.*, vol. 39, no. 5, pp. 3232–3234, Sep. 2003.

[17] M. Kummer, J. Abbott, B. Kratochvil, R. Borer, A. Sengul, and B. J. Nelson, "Octomag: An electromagnetic system for 5-dof wireless micromanipulation," *IEEE Trans. Robot.*, vol. 26, no. 6, pp. 1006–1017, Dec. 2010.

[18] L. Rossini, O. Chetelat, E. Onillon, and Y. Perriard, "Force and torque analytical models of a reaction sphere actuator based on spherical harmonic rotation and decomposition," *IEEE/ASME Trans. Mechatronics*, vol. 18, no. 3, pp. 1006–1018, Jun. 2013.

[19] Y. Liang, C. I-Ming, Y. Guilin, and L. Kok-Meng, "Analytical and experimental investigation on the magnetic field and torque of a permanent magnet spherical actuator," *IEEE/ASME Trans. Mechatronics*, vol. 11, no. 4, pp. 409–419, Aug. 2006.

[20] X. Liu, G. Mancini, and J. Tan, "Design of a unified active locomotion mechanism for a capsule-shaped laparoscopic camera system," in *Proc. IEEE Int. Conf. Robot. Autom.*, 2014, pp. 2449–2456.

[21] X. Liu, G. J. Mancini, and J. Tan, "Design of a unified active locomotion mechanism for a wireless laparoscopic camera system," in *Proc. IEEE/RSJ Int. Conf. Intell. Robots Syst.*, 2014, pp. 1294–1301.

[22] C. Song, A. Alijani, T. Frank, G. Hanna, and A. Cuschieri, "Mechanical properties of the human abdominal wall measured in vivo during insufflation for laparoscopic surgery," *Surg. Endosc. Other Interventional Techn.*, vol. 20, no. 6, pp. 987–990, 2006.

[23] S. Best, W. Kabbani, D. Scott, R. Bergs, H. Beardsley, R. Fernandez, L. Mashaud, and J. Cadeddu, "Magnetic anchoring and guidance system instrumentation for laparo-endoscopic single-site surgery/natural orifice transluminal endoscopic surgery: Lack of histologic damage after prolonged magnetic coupling across the abdominal wall," *Urology*, vol. 77, no. 1, pp. 243–247, 2011.

[24] S. Loring, R. Brown, A. Gouldstone, and J. Butler, "Lubrication regimes in mesothelial sliding," *J. Biomech.*, vol. 38, no. 12, pp. 2390–2396, 2005.

[25] J. D. Jackson, *Classical Electrodynamics*. New York, NY, USA: Wiley, 1999.

[26] L. Kok-Meng and S. Hungsun, "Distributed multipole model for design of permanent-magnet-based actuators," *IEEE Trans. Magn.*, vol. 43, no. 10, pp. 3904–3913, Oct. 2007.
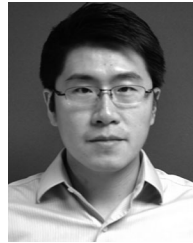
Xiaolong Liu received the B.E. and M.E. degrees in electrical and computer engineering from Northeastern University, Shenyang, Liaoning, China, in 2008 and 2010, respectively, and the Ph.D. degree in biomedical engineering from The University of Tennessee, Knoxville, TN, USA, in 2015.

He is currently an Intern at Smokie Robotics, Inc., Knoxville, where he performs research and development in robotics and automation. His current research interests include surgical robotics, mobile manipulation, and engineering design.

Gregory J. Mancini received the M.D. degree in general surgery from the Mercer University School of Medicine, Macon, GA, USA, in 2000.

He is currently an Associate Professor of surgery at the University of Tennessee, Knoxville, TN, USA. His clinical practice and academic efforts focus on the area of minimally invasive surgery. He presents and teaches extensively both regionally and internationally on the topics of acid reflux, hernia, and bariatric surgery.

Dr. Mancini is board certified in General Surgery by the American Board of Surgery and is a Fellow of the American College of Surgeons. He is active in national surgical societies such as the Society of American Gastrointestinal and Endoscopic Surgeons, the Society of Laparoendoscopic Surgeons, the American Hernia Society, the American College of Surgeons, and the American Society of Metabolic and Bariatric Surgery.

Yong Guan received the Ph.D. degree in computer science from the China University of Mining and Technology, Beijing, China, in 2004.

He is currently a Professor at Capital Normal University, Beijing. His research interests include formal verification, and PHM for power and embedded system design. He is a Member of the Chinese Institute of Electronics Embedded Expert Committee. He is also a Member of the Beijing Institute of Electronics Professional Education Committee and a Standing Council Member of the Beijing Society for Information Technology in Agriculture.

Jindong Tan received the Ph.D. degree in electrical and computer engineering from Michigan State University, East Lansing, MI, USA, in 2002.

He is currently a Professor and the Associate Department Head at the Department of Mechanical, Aerospace and Biomedical Engineering, The University of Tennessee, Knoxville, TN, USA. He has been an Assistant/Associate Professor with the Department of Electrical and Computer Engineering, Michigan Technological University, Houghton, MI. His current research interests include mobile sensor networks, augmented reality and biomedical imaging, dietary assessment, and mobile manipulation.

Dr. Tan is a Member of the ACM and Sigma Xi.